

Beam matching: a method to study phonon transport through interfaces and multilayer structures

Debanjan Basu¹ and Peter E. Blöchl^{1,2}

¹*Institute for Theoretical Physics, Clausthal University of Technology,
Leibnizstr. 10, 38678 Clausthal-Zellerfeld, Germany*

²*Institute for Materials Physics, Georg-August-Universität Göttingen,
Friedrich-Hund-Platz 1, 37077 Göttingen, Germany*

(Dated: August 4, 2021)

Structuring materials is one mechanism to influence the thermal conductivity and thus thermoelectric efficiency. In order to investigate the scattering of phonons in multilayer structures we developed a beam matching technique, which is based on the concept of individual phonons and their scattering at interfaces. One of the major goals is to efficiently determine the complex band structure of the bulk materials. The complex band structure is determined using selected k-points on a triangulated grid in the complex plane of wave vectors perpendicular to the interface. Matching the phonon modes at an interface is translated to a singular value problem. Its null-vectors provide the coupling coefficients of the phonon modes across the interface. Besides giving explicit access to the modes as they scatter at the interface, the technique provides the transfer matrices, that provide the transmission coefficient of any multilayer structure. The transmission coefficient, in turn, yields the phononic thermal conductance for coherent transport. The knowledge of the matched phonons forms the basis of investigating incoherent transport under the influence of phonon-phonon or impurity scattering.

Keywords: complex band structure; phonons; thermal transport; multilayers.

I. INTRODUCTION

Control of thermal conductivity is essential for the development of thermoelectric devices. Thermoelectric efficiency depends on the presence of a large electronic conductivity and a small thermal conductivity. The so-called figure of merit ZT , which describes how efficiently a material can produce thermoelectric power, is given by

$$ZT = \frac{\sigma S^2 T}{\kappa}, \quad (1)$$

where σ is the electric conductivity, S is the Seebeck coefficient, T is the temperature and κ is the thermal conductivity. Besides electrons, phonons are the dominant carriers for thermal conductivity. Because the thermal conductivity due to electrons is closely linked to the electric conductivity via the Wiedemann-Franz law, the decrease of phononic thermal conductivity is one handle to improve the efficiency of thermoelectric devices.

Structuring materials is one possibility to influence the phononic thermal conductivity. The basic structuring element is an interface, which acts like a filter for the impinging phonons. Phonons on one side of the interface will be partially reflected by the interface and partially transmitted across the interface. In certain frequency regions, one of the materials may not support propagating phonons, which completely blocks out the corresponding phonon current. By alternating soft and hard materials, for example, the thermal resistance can be increased above the mean resistance of both materials. The thermal resistance of an interface, called Kapitza resistance¹, produces a finite temperature step across the interface in the presence of a thermal current.

More complex structures involve several interfaces. Multiple reflections between these interfaces enhance or suppress the thermal current due to constructive or destructive interference respectively. These effects depend crucially on the relative phases of individual phonons. Furthermore, the local behavior in structures with small spatial dimensions differs from the near-equilibrium description employed on macroscopic length scales.

This work addresses the transport of phonons across single and multiple interfaces. The tools developed can, however, be extended to the transport of other quasiparticles across single or multiple interfaces. The description accounts for evanescent waves, which mediate phonon tunneling through thin layers of a material, and which can also transport heat across the interface, if additional scattering processes convert the energy into propagating modes. Evanescent waves can combine to form true interface states, that exist only in the proximity of the interface. The methods preserve the phase information, which allows the study of interference effects at multiple interfaces.

The focus on the propagating and evanescent waves as the elementary entities sets this method apart from the atomistic Green's function method²⁻⁶, an elegant and widely used method for phonon transport problems.

The relation between the atomistic Green's function method and our mode-based method is analogous to that of Green's-function based and wave-function based approaches in electronic structure theory. While each method has its own virtues, they can be transformed into each other. For example, the mode coupling coefficients can be extracted from the Greens function⁶.

The advantage of the Green's function method over the present method is the ease with which ensemble averages,

for example over scatterers, are performed. The mode matching described here, in contrast, makes the contact to the individual modes more direct.

The present method also differs from many previous approaches⁷⁻⁹ in that it first evaluates the complex band structure, where it exploits the full symmetry of the bulk materials. These waves are then matched at an interface, which has a reduced symmetry.

In the remainder of this section, we briefly review the theoretical basis of thermal transport via phonons in the incoherent and the coherent limits. Thus we are revisiting the Boltzmann equation on the one hand and the Landauer formula on the other. Both take the complex band structure of the individual materials and the transmission coefficients as the basic input, which are the topic of the present paper. In section II, we relate this description to the motion of individual atoms. These sections serve to introduce our notation. Readers specifically interested in the methodology of calculating the complex band structure and beam matching may skip the introductory sections and return to them whenever the notation needs clarification. In section III we introduce the concept of a complex band structure. The methods have been analyzed using model systems described in section IV. The method for the numerical determination of the complex band structure is presented in section V. In section VI, we describe how the individual solutions are combined at an interface, and how the resulting transfer matrices can be used to determine the transmission through complex multilayer structures. In section VII we describe how to extract the conductance and explore their spectral distribution for a model interface.

A. Thermal conductivity from the phonon-Boltzmann equation

The thermal conductivity tensor κ relates the heat-current density \vec{j}_Q to the temperature gradient $\vec{\nabla}T$,

$$\vec{j}_Q = \sum_{\lambda} n_{\lambda} \epsilon_{\lambda} \vec{v}_{\lambda} = -\kappa \vec{\nabla}T, \quad (2)$$

where n_{λ} is the local phonon density in the mode specified by λ . $\lambda = (\vec{k}, \sigma)$ combines the quantum numbers of a phonon, namely its wave vector \vec{k} and band index σ . The energy of a phonon $\epsilon_{\sigma}(\vec{k}) = \hbar\omega_{\sigma}(\vec{k})$ and its velocity $\vec{v}_{\sigma}(\vec{k}) = \vec{\nabla}_{\vec{k}}\omega_{\sigma}(\vec{k})$ are obtained from the dispersion relation, that is, the phonon band structure $\omega_{\sigma}(\vec{k})$.

The phonon occupations in a temperature gradient can be extracted from the phonon-Boltzmann equation^{10,11}, which describes the dynamics of the phonon densities $n_{\lambda}(\vec{r}, t)$ in space and time. After linearizing the scattering term in the deviation of the phonon densities from their equilibrium values, the resulting linearized phonon-Boltzmann equation is

$$\frac{\partial n_{\lambda}}{\partial t} + \vec{v}_{\lambda} \vec{\nabla} n_{\lambda} = - \sum_{\lambda'} B_{\lambda, \lambda'} \left(n_{\lambda'} - n_{\lambda'}^{eq}(T) \right). \quad (3)$$

The first order of the scattering term in deviations from thermal equilibrium defines \mathbf{B} as

$$B_{\lambda, \lambda'} = - \left. \frac{\partial}{\partial n_{\lambda'}} \right|_{n^{eq}(T)} \left(\frac{dn_{\lambda}}{dt} \right)_{\text{scatt}}. \quad (4)$$

The equilibrium phonon density $n_{\lambda}^{eq} = n_{\lambda}^0 [e^{\beta\epsilon_{\lambda}} - 1]^{-1}$ is given by the Bose distribution and the density n_{λ}^0 of a single phonon in mode λ . The latter is described in the discussion following Eq. 22 below. As usual, $\beta = 1/(k_B T)$.

For stationary distributions n_{λ} , the thermal current can be extracted from Eqs. 2 and 3

$$\vec{j}_Q = \sum_{\lambda} n_{\lambda} \epsilon_{\lambda} \vec{v}_{\lambda} = - \sum_{\lambda, \lambda'} \epsilon_{\lambda} \vec{v}_{\lambda} B_{\lambda, \lambda'}^{-1} \left(\vec{v}_{\lambda'} \vec{\nabla} n_{\lambda'} \right). \quad (5)$$

The equilibrium distribution does not show up, because it does not contribute any net currents. With $\vec{\nabla} n_{\lambda} = \frac{dn_{\lambda}^{eq}}{dT} \vec{\nabla}T$, the thermal conductivity tensor is obtained,

$$\kappa = \sum_{\lambda, \lambda'} B_{\lambda, \lambda'}^{-1} \epsilon_{\lambda} \frac{dn_{\lambda}^{eq}}{dT} \vec{v}_{\lambda} \otimes \vec{v}_{\lambda'}, \quad (6)$$

where \otimes denotes the outer product $(\vec{a} \otimes \vec{b})_{i,j} = a_i b_j$.

Considering only the diagonal elements of \mathbf{B}^{-1} in the phonon modes, one obtains the well known relation^{11,12} for thermal conductivities

$$\kappa = \sum_{\lambda} C_{\lambda} \tau_{\lambda} \vec{v}_{\lambda} \otimes \vec{v}_{\lambda}, \quad (7)$$

where $\tau_{\lambda} = (\mathbf{B}^{-1})_{\lambda, \lambda}$ can be identified with the relaxation time, respectively the phonon lifetime. $C_{\lambda} = \epsilon_{\lambda} dn_{\lambda}^{eq}(T)/dT$ is the contribution of a phonon mode to the heat capacity per unit volume. A graph of C_{λ} is shown in Fig. 1. Its main effect is to cut off the high-frequency phonons at low temperatures, i.e. below the Debye temperature.

Among the main bulk scattering processes are impurity scattering, electron-phonon scattering and the temperature dependent phonon-phonon scattering¹³⁻¹⁵.

One of the central approximations of the Boltzmann equation is that the phase information of phonons is lost between two scattering events. The phase information is responsible for quantum mechanical interference effects. This approximation implies that the typical scattering length needs to be larger than the coherence length.

The importance of this limitation is evident from the two possible descriptions of a multilayer. One uses the modes of the multilayer. The other uses the modes of the individual layers and the transmission coefficients across the interfaces. The first description takes coherent multiple scattering between interfaces fully into account, while the second suppresses this effect by introducing a phase average after each interface traversal. Applying the Boltzmann equation to multilayer systems is thus not unique. It needs to be done with attention to the relevant decoherence mechanisms and dissipation channels.

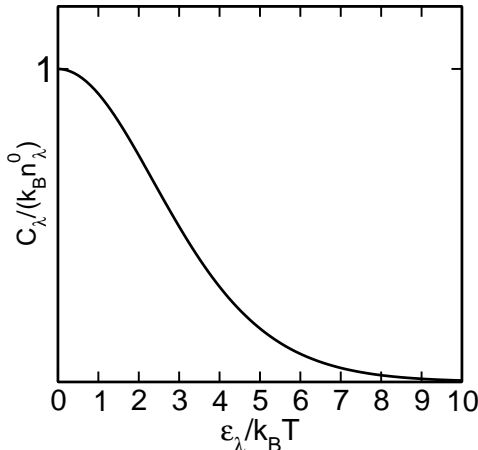


FIG. 1. Heat capacity C_λ per volume of a phonon mode as function of the phonon energy ϵ_λ .

B. Thermal conductance from ballistic transport

The assumptions of the Boltzmann equation require that the length scale of structured materials is larger than the coherence length of the phonons. For materials with structures on the nano-scale the underlying assumptions of the Boltzmann equation are often violated.

The opposite extreme to the incoherent transport described by the Boltzmann equation is ballistic transport. In coherent or ballistic transport, multiple scattering is considered, i.e. scattering events cannot be disentangled because they occur within the coherence length of the scattered particle.

The heat current I_Q through the material structure is related to the temperature difference ΔT at the contacts by the conductance G .

$$I_Q = G\Delta T \quad (8)$$

The thermal conductance of a homogeneous block of material can be expressed by its thermal conductivity κ as $G = \frac{A}{\ell}(\vec{e}\kappa\vec{e})$, where A is the cross section of the material, ℓ is its length, and \vec{e} is the normal vector of the cross-section plane.

The ballistic heat current is obtained assuming that the density n_λ of incoming phonons in each contact is identical to the equilibrium density $n_\lambda^{eq}(T)$ at the temperature of that contact. The outgoing phonon fluxes are related to the incoming phonon fluxes by the reflection and transmission coefficients: the transmission coefficient $\mathcal{T}_{\lambda,\lambda'}$ is the ratio between the flux of transmitted phonons in mode λ' and the flux of incoming phonons in mode λ . Similarly, the reflection coefficient $\mathcal{R}_{\lambda,\lambda'}$ is the ratio between the flux of reflected phonons in mode λ' and the flux of incoming phonons in mode λ . The reflection and transmission coefficients account for all multiple

scattering events inside the material.

The ballistic heat current from contact A to contact B is

$$I_Q = A_A \sum_{\lambda \in A, \lambda' \in B} \theta(\vec{e}\vec{v}_\lambda) n_\lambda^{eq}(T_A) (\vec{e}\vec{v}_\lambda) \epsilon_\lambda \mathcal{T}_{\lambda,\lambda'}^{A \rightarrow B} - A_B \sum_{\lambda \in A, \lambda' \in B} \theta(\vec{e}'\vec{v}_{\lambda'}) n_{\lambda'}^{eq}(T_B) (\vec{e}'\vec{v}_{\lambda'}) \epsilon_{\lambda'} \mathcal{T}_{\lambda',\lambda}^{B \rightarrow A}, \quad (9)$$

where $\theta(x)$ is the Heaviside step function, which is unity for positive arguments and which vanishes for negative arguments. It selects the phonons in the incoming direction. A_A is the cross section of contact A and \vec{e} is its plane normal pointing inward. Similarly, A_B is the cross section of material B with the plane normal \vec{e}' pointing inward. We exploited that reflection and transmission coefficients add up to one, i.e.

$$\sum_{\lambda' \in A} \mathcal{R}_{\lambda,\lambda'}^{A \rightarrow A} + \sum_{\lambda' \in B} \mathcal{T}_{\lambda,\lambda'}^{A \rightarrow B} = 1, \quad (10)$$

in order to relate the unidirectional flux to the transmitted fluxes.

For equal temperatures, i.e. $T_A = T_B$, the thermal current vanishes, which relates the right-going flux to the left-going flux at the same temperature. This notion allows to simplify the expression for the heat current by replacing the difference of left- and right-going fluxes by the differences of two right-going fluxes at two different temperatures.

$$I_Q = A_A \sum_{\lambda \in A} \left(n_\lambda^{eq}(T_A) - n_\lambda^{eq}(T_B) \right) \epsilon_\lambda \times \sum_{\lambda' \in B} \theta(\vec{e}\vec{v}_\lambda) (\vec{e}\vec{v}_\lambda) \mathcal{T}_{\lambda,\lambda'}^{A \rightarrow B} \quad (11)$$

For small temperature differences $T_A - T_B$, the equilibrium occupations can be linearized in temperature so that we obtain the thermal conductance G from Eqs. 8 and 11 as

$$G = A_A \sum_{\lambda \in A} C_\lambda \sum_{\lambda' \in B} \theta(\vec{e}\vec{v}_\lambda) (\vec{e}\vec{v}_\lambda) \mathcal{T}_{\lambda,\lambda'}^{A \rightarrow B}. \quad (12)$$

$C_\lambda = \epsilon_\lambda \frac{\partial}{\partial T} n_\lambda^{eq}$ also occurred in the expression Eq. 7 for the thermal conductivity. It is the contribution of the phonon mode λ to the heat capacity per volume. It is evaluated at the mean temperature $T = \frac{1}{2}(T_A + T_B)$ of the two contacts.

The basic quantities determining the thermal current due to phonons are (1) the phonon dispersion relation $\omega_\sigma(\vec{k})$, (2) the equilibrium phonon distribution $n^{eq}(T)$, (3) the matrix \mathbf{B} describing incoherent scattering and (4) the transmission coefficients \mathcal{T} for ballistic transport.

The limitations of Eq. 12 for the conductance have been pointed out by Simons¹⁶ and further extended by others¹⁷⁻¹⁹: Eq 12 predicts a finite thermal resistance even for an interface between identical materials. This paradox is resolved by including on both sides the deviations $n_\lambda - n_\lambda^{eq}(T)$ from thermal equilibrium occupations as obtained from the Phonon-Boltzmann equation Eq. 3.

II. EQUATIONS OF ATOMIC MOTION AND PHONONS

The theory presented so far uses the phonon density n_λ as the basic quantity. Here we establish contact of the phonon distribution with the dynamics of individual atoms.

Let us start from the Newton's equations of motion for the atoms in a crystal. We denote the atomic coordinates by $R_{i,\vec{r}}$, where $i = 1, \dots, 3N$ and N is the number of atoms in a unit cell. With \vec{r} we denote the lattice vectors $\vec{r}_{i,j,k} = \vec{T}_1 i + \vec{T}_2 j + \vec{T}_3 k$ given by the three primitive translation vectors $\vec{T}_1, \vec{T}_2, \vec{T}_3$ of the crystal and integer i, j, k .

The potential energy is given by the energy surface $V(\vec{R})$, which depends on all atomic positions in the crystal. Expanding the total energy in a Taylor expansion about a minimum up to second order provides the force constants $c_{i,\vec{r},j,\vec{r}'} = \frac{\partial^2 V}{\partial R_{i,\vec{r}} \partial R_{j,\vec{r}'}}$. The force constants define the phonon modes, whereas higher-order terms in this Taylor expansion describe phonon-phonon scattering.

The Lagrangian for the displacements $u_{i,\vec{r}}$ from the equilibrium positions is

$$\mathcal{L} = \frac{1}{2} \sum_{i,\vec{r}} m_i \dot{u}_{i,\vec{r}}^2 - \frac{1}{2} \sum_{i,j,\vec{r},\vec{r}'} u_{i,\vec{r}} c_{i,\vec{r},j,\vec{r}'} u_{j,\vec{r}'}, \quad (13)$$

where m_i are the atomic masses. The sum over lattice translation vectors \vec{r} includes \mathcal{N} unit cells.

The equations of motion for the displacements are obtained as Euler-Lagrange equations $\frac{d}{dt} \frac{\partial \mathcal{L}}{\partial \dot{u}_{i,\vec{r}}} - \frac{\partial \mathcal{L}}{\partial u_{i,\vec{r}}} = 0$, which yields

$$m_i \ddot{u}_{i,\vec{r}} = - \sum_{j,\vec{r}'} c_{i,\vec{r},j,\vec{r}'} u_{j,\vec{r}'}. \quad (14)$$

The discrete translational symmetry of a crystal is reflected in the equation

$$c_{i,\vec{r},j,\vec{r}'} = c_{i,\vec{r}+\vec{t},j,\vec{r}'+\vec{t}} \quad (15)$$

for the force constants. The eigenvalue for a translation by \vec{t} is $e^{i\vec{k}\vec{t}}$, which is expressed by the wave vector \vec{k} .

The displacements can be described by the eigenmodes of the lattice translation operator in the form

$$u_{i,\vec{r}}(t) = \frac{1}{\sqrt{\mathcal{N}}} \sum_{\vec{k},\sigma} \frac{1}{\sqrt{m_i}} U_{i,\sigma}(\vec{k}) e^{i\vec{k}\vec{r}} Q_\sigma(\vec{k}, t), \quad (16)$$

where $Q_\sigma(\vec{k}, t)$ are the mode amplitudes. The sum contains \mathcal{N} wave vectors. The mode amplitudes are related to each other by the condition $Q^*(\vec{k}, t) = Q(-\vec{k}, t)$, enforcing real displacements.

The parameters $U_{i,\sigma}(\vec{k})$ for a given band index σ and wave vector \vec{k} are normalized eigenvectors of the dynamical matrix

ical matrix

$$D_{i,j}(\vec{k}) = \sum_{\vec{r}} \frac{c_{i,\vec{r},j,\vec{r}} e^{i\vec{k}\vec{r}}}{\sqrt{m_i m_j}}. \quad (17)$$

They are chosen so that $U_{i,\sigma}(\vec{k}) = U_{i,\sigma}^*(-\vec{k})$. The squared angular frequencies $\omega_\sigma^2(\vec{k})$ are the eigenvalues of the dynamical matrix, that is

$$\sum_{j=1}^{3N} D_{i,j}(\vec{k}) U_{j,\sigma}(\vec{k}) = U_{i,\sigma}(\vec{k}) \omega_\sigma^2(\vec{k}). \quad (18)$$

One outcome is the dispersion relation, i.e. the angular frequency $\omega_\sigma(\vec{k})$ as function of wave vector and the index σ for a particular phonon branch. It yields the phonon energy $\epsilon_\sigma(\vec{k}) = \hbar \omega_\sigma(\vec{k})$ and the group velocity $\vec{v}_\sigma(\vec{k}) = \vec{\nabla}_{\vec{k}} \omega_\sigma(\vec{k})$.

In terms of the mode amplitudes $Q_\sigma(\vec{k}, t)$, the Lagrangian can be expressed in terms of individual harmonic oscillators.

$$\mathcal{L} = \sum_{\vec{k},\sigma} \frac{1}{2} \left[\dot{Q}_\sigma^*(\vec{k}) \dot{Q}_\sigma(\vec{k}) - \omega_\sigma^2(\vec{k}) Q_\sigma^*(\vec{k}) Q_\sigma(\vec{k}) \right] \quad (19)$$

The mode amplitudes can be written as

$$Q(\vec{k}, t) = \sqrt{\frac{\hbar}{\omega_\sigma(\vec{k})}} \times \left(b_\sigma(\vec{k}) e^{-i\omega_\sigma(\vec{k})t} + b_\sigma^*(-\vec{k}) e^{+i\omega_\sigma(\vec{k})t} \right). \quad (20)$$

While the coefficients $Q_\sigma(\vec{k})$ describe waves travelling in opposite directions, Eq. 20 rearranges the modes such that the phonon amplitudes $b_\sigma(\vec{k}, t)$ describe waves that travel along only one specific direction.

The total energy is a sum over the individual phonons

$$E = \sum_{\vec{k},\sigma} \hbar \omega_\sigma(\vec{k}) b_\sigma^*(\vec{k}) b_\sigma(\vec{k}) \quad (21)$$

so that the phonon density of a mode $\lambda = (\vec{k}, \sigma)$,

$$n_\lambda = \frac{1}{\mathcal{N} \Omega_T} b_\lambda^* b_\lambda, \quad (22)$$

can be expressed by the absolute square of the phonon amplitudes b_λ . Ω_T is the volume of a real-space unit cell. The constant $n_\lambda^0 = 1/(\mathcal{N} \Omega_T)$ is the density per phonon in mode λ .

Note, that Eqs. 21 and 22 are still purely classical expressions. In a quantum description, the phonon amplitudes translate into creation and annihilation operators and the energies would be shifted by the zero-point energy. The thermal average of the squared amplitudes $b_\lambda^* b_\lambda$ is replaced by the statistical expectation value of the corresponding quantum expression, namely the Bose distribution $\langle b_\lambda^\dagger b_\lambda \rangle_T = [e^{\beta \epsilon_\lambda} - 1]^{-1}$.

III. INTERFACES AND COMPLEX BAND STRUCTURE

A. Conservation of k_{\parallel} at interfaces

If a material has an internal interface or a surface, the translational symmetry perpendicular to the interface or surface is broken. Thus, modes with different wave vectors \vec{k}_{\perp} perpendicular to the surface are no more independent. However, one can still characterize the solutions by the wave-vector components parallel to this plane, described by \vec{k}_{\parallel} .

The fact that \vec{k}_{\parallel} is a preserved quantity, allows one to break down the problem of a multilayer structure with parallel interfaces into many quasi-one-dimensional problems, one for each value of \vec{k}_{\parallel} . The possibility to divide the problem into effective one-dimensional problems is an enormous simplification and will be exploited even when this symmetry is weakly broken.

In order to judge the relevance of the k_{\parallel} selection rule, one should distinguish the two-dimensional surface unit cell of the individual half-crystals from the two-dimensional unit cell of the interface: Depending on the registry of the two half-crystals, the interface unit cell may contain several surface unit cells of each half-crystal.

Interesting is the point of view of one particular half crystal. An incoming phonon with a parallel wave vector \vec{k}_{\parallel} in the surface reciprocal unit cell of one half crystal produces reflected phonons not only for the same value of \vec{k}_{\parallel} , but also for any vector $\vec{k}_{\parallel} + \vec{g}_{\parallel,1}^T i + \vec{g}_{\parallel,2}^T j$ shifted by a reciprocal lattice vector of the interface. A poor fit of the two lattices implies a large real-space interface unit cell and hence small reciprocal lattice vectors for the interface.

As the interface becomes more complex, i.e. for larger interfacial unit cells, the spacing of this grid of reciprocal interfacial lattice vectors decreases. Thus, in the limit of an incommensurate interface this grid covers all space, which renders the selection rule meaningless.

B. Complex wave vectors and complex band structure

In an extended material, only modes with real wave vectors are of relevance, because only these lead to finite amplitudes in an infinite crystal. At an interface, however, we also need to consider modes that fall off towards the interior of the material²⁰. Such evanescent modes either couple to extended modes on the other side of the interface, or they form interface states that fall off in both directions away from the interface.

These are modes with complex perpendicular wave vector k_{\perp} . They describe wave functions that fall off exponentially away from the interface. Each of these evanescent modes has a partner that falls off in the opposite direction.

A dispersion relation $\omega_{\sigma}(\vec{k})$ that considers not only the extended solutions with real wave vector, but also those with complex wave vector is called a *complex band structure*^{21,22}. For a given k_{\parallel} , a complex band structure consists of lines in the three-dimensional $(\text{Re}(\omega), \text{Re}(k_{\perp}), \text{Im}(k_{\perp}))$ space. An example of a complex band structure alongside with sketches of the corresponding displacement fields is shown in Fig. 2.

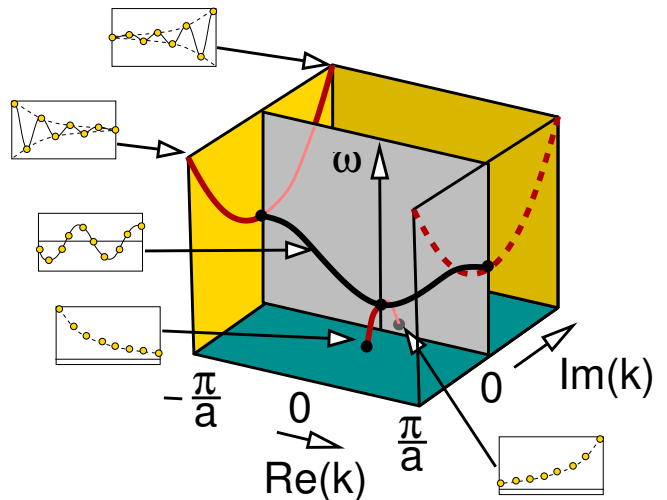


FIG. 2. Complex band structure for the one-dimensional hanging linear chain described in section IV A. The black line is the real band structure, which describes extended solutions. The black and red lines together form the complex band structure. The solutions with complex wave vector have either an exponential decay or growth. The band structure is periodic in the $\text{Re}(k_{\perp})$ direction. The dashed red line is a periodic replica of the red line at the other Brillouin-zone boundary.

C. Complex eigenvalue problem

The dynamical matrix for complex wave vectors is not necessarily hermitian. As a result, the eigenvalues are not real-valued and the eigenvectors are not orthogonal. Rather, the eigenvalues $\omega_{\sigma}^2(\vec{k})$ are complex, and there are distinct left-handed and right-handed eigenvectors. Nevertheless, left-handed eigenvectors $\vec{y}_{\sigma}^{(L)}$ and right-handed eigenvectors $\vec{y}_{\sigma}^{(R)}$ are still related by a bi-orthogonality condition, i.e.

$$\left(\vec{y}_{\sigma}^{(L)}\right)^* \vec{y}_{\sigma'}^{(R)} = 0 \quad \text{for } \sigma \neq \sigma', \quad (23)$$

which allows one to construct one set from the other by a matrix inversion and subsequent normalization.

Diagonalization of the dynamical matrix with a given real wavevector \vec{k}_{\parallel} in the interface plane and a complex wave vector k_{\perp} perpendicular to the plane yields

$$\omega_{\sigma}^2(\vec{k}_{\parallel}, \text{Re}(k_{\perp}), \text{Im}(k_{\perp})) \quad (24)$$

with a complex-valued squared frequency ω_σ^2 . In the following we will use the term complex band structure also for this object.

IV. MODEL SYSTEMS

In order to demonstrate the principles and the working of the method we have chosen three model systems, namely the hanging linear chain, the cubic spring model and a one-dimensional multi-band model that avoids high symmetries.

A. Hanging linear chain

A minimal model for a phonon dispersion relation is the hanging linear chain. The hanging linear chain is a one-dimensional chain of pendula connected by springs.

In contrast to the conventional linear chain, the real band structure of the hanging linear chain has a minimum frequency above zero. This qualitative feature is typical for the quasi-one-dimensional problems resulting from interfaces with non-zero wave vector in the plane $k_{||}$. While the acoustic phonon branch of a three-dimensional phonon band structure reaches down to zero at $k_{||} = 0$, the band structure for $k_{||} \neq 0$ has a non-zero minimum frequency.

We start from a Lagrangian

$$\mathcal{L} = \sum_{j=-\infty}^{\infty} \left[\frac{1}{2} m \dot{u}_j^2 - \frac{1}{2} c (u_{j+1} - u_j)^2 - \frac{1}{2} b u_j^2 \right], \quad (25)$$

where the first term describes the kinetic energy and the remaining terms are, with opposite sign, the potential energies stored in the springs and pendula.

The equation of motion is

$$m \ddot{u}_j = c (u_{j+1} - 2u_j + u_{j-1}) - b u_j, \quad (26)$$

where j is the index of the bead along the chain. With a lattice constant a , the equilibrium position of the j -th bead is at ja . The term $-b u_j$ is the linearized restoring force of the pendulum.

The dynamical matrix depends on the complex wave vector k , which corresponds to k_{\perp} in a three-dimensional problem. The eigenvalues of the dynamical matrix for this system are

$$\omega^2(k) = \frac{b}{m} + \frac{2c}{m} (1 - \cos(ka)), \quad (27)$$

where a is the lattice constant, respectively the spacing of the beads. This complex band structure is shown schematically in Fig. 2.

The complex band structure is given by

$$k = \pm \begin{cases} \frac{i}{a} \operatorname{arccosh}(F(\omega)) & \text{for } \omega < \sqrt{\frac{b}{m}} \\ \frac{1}{a} \arccos(F(\omega)) & \text{for } \sqrt{\frac{b}{m}} < \omega < \sqrt{\frac{b+4c}{m}} \\ \frac{\pi}{a} + \frac{i}{a} \operatorname{arccosh}(-F(\omega)) & \text{for } \omega > \sqrt{\frac{b+4c}{m}} \end{cases} \quad (28)$$

with $F(\omega) = \frac{b+2c-m\omega^2}{2c}$. Because the dynamical matrix is a scalar, its eigenvector $U_{j,\sigma}(k)$ used in Eq. 16 is a number, namely one.

Let us highlight two observations^{21,22} that we will return to in the following.

1. the number of bands are the same for all frequencies. (In this case two.);
2. bands emerge into the complex plane at the extrema of the real band structure.

B. Cubic spring model

In order to go beyond one-dimensional models, we use the cubic spring model. This model consists of atoms arranged on a simple cubic lattice with nearest-neighbor bond stretch and bond bend terms. The high symmetry of the model simplifies calculations.

The lattice constants are $\vec{T}_1 = (a, 0, 0)$, $\vec{T}_2 = (0, a, 0)$ and $\vec{T}_3 = (0, 0, a)$.

The Lagrangian is given by Eq. 13 for one atom per unit cell, i.e. $i, j \in \{1, 2, 3\}$, and the force constant matrix

$$c_{i,\vec{0},j,\vec{k}} = \delta_{i,j} \left[c \left(\delta_{\vec{i},\vec{T}_i} - 2\delta_{\vec{i},\vec{0}} + \delta_{\vec{i},-\vec{T}_i} \right) + \bar{c} \sum_{k \neq i} \left(\delta_{\vec{i},\vec{T}_k} - 2\delta_{\vec{i},\vec{0}} + \delta_{\vec{i},-\vec{T}_k} \right) \right]. \quad (29)$$

The spring constant c describes the force constant for bond stretching and determines the longitudinal speed of sound. The spring constant \bar{c} on the other hand describes the force constant for bond bending and determines the transversal speed of sound.

Below, we use this model to calculate the spectral distribution of the conductance for the current from material A to material B . The parameters are $m^A = m^B = 1$, $a^A = a^B = 1$, $c^A = 0.125$, $\bar{c}^A = 0.05$, $c^B = 0.075$, $\bar{c} = 0.02$, where the super script indicates the respective material at the interface. The spring constant across the interface are the average spring constants of both materials.

The eigenvalues of the dynamical matrix are

$$\omega_\sigma^2(\vec{k}) = \frac{2c}{m} (1 - \cos(k_\sigma a)) + \sum_{\sigma'; \sigma' \neq \sigma} \frac{2\bar{c}}{m} (1 - \cos(k_{\sigma'} a)), \quad (30)$$

where σ is one of the three polarization directions. The eigenvectors of the dynamical matrix are $U_{i,\sigma}(\vec{k}) = \delta_{i,\sigma}$.

For an interface parallel to one of the cubic lattice planes, the band structure along for k_{\perp} can be mapped for each k_{\parallel} onto the hanging linear chain described above. The parameters are given in table I.

polarization	c	b
(1,0,0)	\bar{c}	$2c \cos(k_x a) + 2\bar{c} \left(1 - \cos(k_y a)\right)$
(0,1,0)	\bar{c}	$2\bar{c} \cos(k_x a) + 2c \left(1 - \cos(k_y a)\right)$
(0,0,1)	c	$2\bar{c} \cos(k_x a) + 2\bar{c} \left(1 - \cos(k_y a)\right)$

TABLE I. Parameters (b, c) for the hanging linear chain model described in section IV A, equivalent to the cubic spring model with parameters c, \bar{c} for a given interface wave vector $k_{\parallel} = (k_x, k_y)$. The masses m and lattice constants a of both systems are identical.

C. One-dimensional 3-band model

A third model system is used for testing the numerical methods for complex band structure. This model has been devised to contain several qualitative features present in real systems such as (1) several extrema in real bands (2) loops in the complex plane that connect two bands at different real wave vector and (3) more than the minimum number (2) of vertical bands. Thus, this model lacks a number of symmetry-dictated properties of the hanging linear chain.

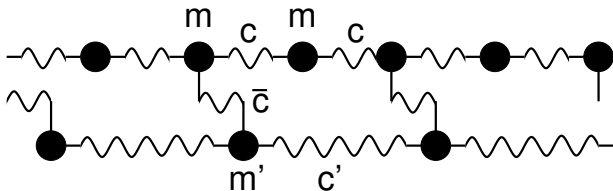


FIG. 3. Sketch of the 3-band model described in section IV C.

The model consists of two coupled linear chains: One of the chains is described by the Lagrangian

$$\mathcal{L}_1 = \sum_j \left(\frac{1}{2} \sum_{i=1}^2 m \dot{u}_{i,j}^2 - \frac{1}{2} c (u_{1,j} - u_{2,j})^2 + \frac{1}{2} c (u_{2,j} - u_{1,j+1})^2 \right). \quad (31)$$

It has two atoms in the unit cell and produces one acoustic and one optical branch. The other chain, described by the Lagrangian

$$\mathcal{L}_2 = \sum_j \left(\frac{1}{2} m' \dot{u}_{3,j}^2 - \frac{1}{2} c' (u_{3,j} - u_{3,j+1})^2 \right) \quad (32)$$

has only one atom per cell and thus contributes only an acoustic branch. A spring couples the second chain to every second bead of the first chain.

$$\mathcal{L}_3 = \sum_j \left(-\frac{1}{2} \bar{c} (u_{1,j} - u_{3,j})^2 \right) \quad (33)$$

The coupling avoids the crossings and results in three distinct bands in the real band structure.

The total Lagrangian $\mathcal{L} = \mathcal{L}_1 + \mathcal{L}_2 + \mathcal{L}_3$ is the sum of the three terms. All parameters of the model, m, m', c, c', \bar{c} , are set equal to one.

The complex band structure of this system has been calculated with the methods described below and is shown in Fig. 7.

V. NUMERICAL DETERMINATION OF THE COMPLEX BAND STRUCTURE

The numerical methods for evaluating the complex band structure of phonons are closely related to those for electrons. The standard method to determine the complex band structure is the eigenvalue method developed by Chang and Shulman^{7,8}. It has been used to describe the complex band structure of electrons and has later been extended to phonons⁹. The eigenvalue method is an efficient method to determine the complex bands energy by energy. In contrast, the method described below follows the complex bands in complex k_{\perp} -plane. Thus our method seems suitable for the description of phonon transport, which is, unlike electrons, not limited to a small energy region near a Fermi surface.

A. Triangulation

In order to address the problem numerically, we define a discrete grid of points in the complex k_{\perp} -plane. The region in between the grid points is triangulated, so that the triangles fill the complex k_{\perp} plane up to a minimum negative and a maximum positive imaginary value. As shown in Fig. 4, the triangles are arranged with a mirror symmetry in the real axis in order to exploit the corresponding symmetry of the complex band structure.

Inside each triangle, ω_{σ}^2 is linearized. Thus, the information at the grid points is sufficient to determine the triangulated ω_{σ}^2 surfaces completely.

This linearization is the main numerical approximation in the method. It can easily be controlled by choosing a finer grid. In the following, the dispersion relation is replaced by its triangulated approximation, which simplifies the topology of the complex band structure and rigorously avoids certain crossings of complex bands.

The diagonalization of the dynamical matrix for a given grid point k_{\perp} is one of the most time critical steps in the calculation. Only a small fraction of the grid points in the complex k_{\perp} plane is visited, however, so that the

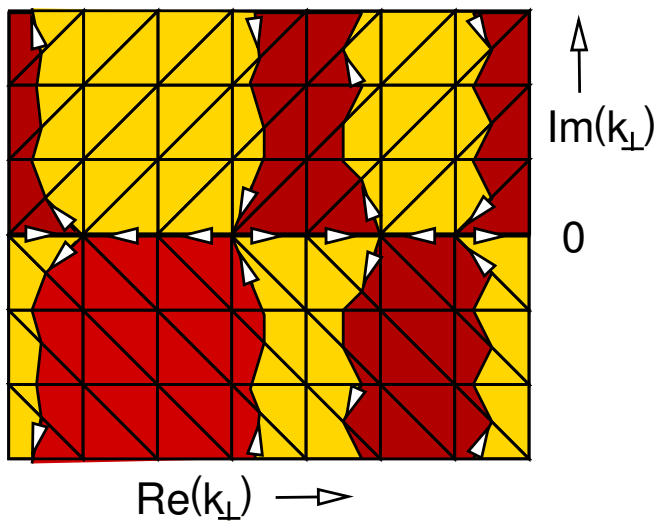


FIG. 4. Triangulation of the complex k_{\perp} plane. The regions with different color indicate the different signs of $\text{Im}(\omega_{\sigma}^2)$ for a specific band index σ . The real part $\text{Re}(\omega_{\sigma}^2)$ of the squared frequencies increases counterclockwise around the dark regions with positive imaginary part $\text{Im}(\omega_{\sigma}^2)$ as indicated by the arrows.

diagonalization need not be performed for all grid points. Rather, the diagonalization for a given k_{\perp} point is performed only when needed. Once obtained, the information is kept for later use.

B. Branch cuts and spurious bands

Frequencies with a finite imaginary part describe solutions that either decay or grow exponentially with time. They are of no interest for our problem. Thus our first task is to find lines in the complex k_{\perp} -plane with $\text{Im}(\omega_{\sigma}^2) = 0$.

At this point, one faces the problem that the choice of the branch index σ is not unique. Common library routines return eigenvalues ordered with increasing real part. For this choice, we find that the imaginary part of ω_{σ}^2 is discontinuous and the real part has discontinuous derivatives. Such a jump of $\text{Im}(\omega_{\sigma}^2)$, which changes its sign, produces spurious solutions of $\text{Im}(\omega_{\sigma}^2) = 0$.

The behavior described above, namely the existence of branch cuts, is typical for avoided band crossings and characteristic of the way different branches of the complex band structure are connected to each other.

Let us therefore demonstrate the behavior for an idealized avoided band crossing in greater detail for a minimal model of the dynamical matrix which depends linearly on the complex k_{\perp} , namely

$$D(k_{\perp}) = \begin{pmatrix} k_{\perp} & 1 \\ 1 & -k_{\perp} \end{pmatrix} \quad (34)$$

The characteristic equation yields $\omega^2 = \pm\sqrt{k_{\perp}^2 + 1}$. The result for real and imaginary part of ω^2 in the complex plane and the resulting complex bands are shown in Fig. 5.

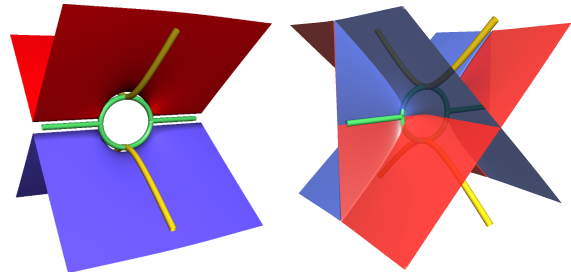


FIG. 5. Real (left) and imaginary part (right) of the squared frequency $\omega^2 = \pm\sqrt{k_{\perp}^2 + 1}$ at an avoided crossing. The real parts of the two branches are shifted vertically by a small amount to make the complex bands visible. The band for real k_{\perp} is shown in yellow, while the one extending into the complex plane is shown in green. The bands pointing horizontally away from the green circle are spurious bands.

In this example, the lines with $\text{Im}(\omega_{\sigma}^2) = 0$ are the two orthogonal lines with either $\text{Re}(k_{\perp}) = 0$ or $\text{Im}(k_{\perp}) = 0$. At the line, where the two sheets of $\text{Re}(\omega_{\sigma}^2(k_{\perp}))$ cross, i.e. at $\text{Re}(k_{\perp}) = 0$ and $|\text{Im}(k_{\perp})| > 1$, the imaginary part of ω_{σ}^2 exhibits a discontinuity and each sheet of $\text{Im}(\omega_{\sigma}^2(k_{\perp}))$ changes its sign. At the onset of this discontinuity, i.e. at $k_{\perp} = \pm i$, are the points in the complex k_{\perp} plane, where the complex bands connect from one sheet to the other. These are also the points where the branch cut, respectively the discontinuity of the imaginary part of ω^2 start to develop, and where the spurious bands, the straight sections of the green lines, lie.

The two ω_{σ}^2 sheets are multiply connected. Trying to treat them individually causes discontinuities either in the real part or the imaginary part of ω^2 surfaces. Where exactly these discontinuities lie, depends on the way the frequencies are attributed to different bands. However, the discontinuities can not be avoided altogether when separating different bands.

Treating all bands together from the outset makes the concepts rather complicated. A surprisingly simple solution to this problem has been to ignore the problem at first and to divide the bands according to increasing $\text{Re}(\omega_{\sigma}^2(k_{\perp}))$ into different sheets. Then, the complex bands are extracted for each sheet individually. This introduces on the one hand spurious bands, which, on the other hand, are easily removed later on, when the band from different sheets are connected.

C. Analytic properties of the complex band structure and vertical bands

The analytic properties of the complex band structure for the one-dimensional Schrödinger equation has been

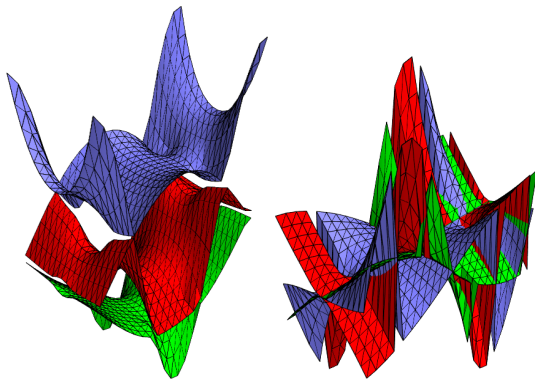


FIG. 6. Real part (left) and imaginary part (right) of ω_σ^2 in the complex k_\perp -plane. If the eigenvalues of the dynamical matrix are ordered with respect to increasing real part, the imaginary part is connected in a discontinuous manner. The resulting sign changes produce spurious bands that need to be removed.

analyzed by Kohn²¹. Heine²² generalized the results to higher dimensions. They are summarized for example by Yip and Chang⁹.

The complex band structure has a mirror symmetry of the real part and a mirror antisymmetry of the imaginary part of ω_σ^2 at the plane with $\text{Im}(k_\perp) = 0$, i.e. $\omega_\sigma^2(k_\perp) = (\omega_\sigma^2(k_\perp^*))^*$, where z^* denotes the complex conjugate of z .^{9,23}

From the Cauchy-Riemann equations for a given band ω_σ^2 follows that the condition $\text{Im}[\omega_\sigma^2] = 0$ determines directions of steepest descent of $\text{Re}[\omega_\sigma^2(\vec{k}_\perp)]$. The path following the gradient of $\text{Re}[\omega_\sigma^2(\vec{k}_\perp)]$ proceeds in counter-clockwise direction around a region with $\text{Im}[\omega_\sigma^2] > 0$. The monotonous growth of a $\text{Re}[\omega_\sigma^2(\vec{k}_\perp)]$ while circling around a region with positive $\text{Im}[\omega_\sigma^2]$ excludes disconnected regions with one sign of the imaginary part, which in turn excludes disconnected complex bands. These properties do not hold on a branch cut, which violates the Cauchy-Riemann equations.

The finding above indicates that the topology of the complex band structure can be comprehended reasonably well by exploring the regions in the complex plane with $\text{Im}[\omega_\sigma^2] > 0$.

An important consequence of the above is that branches of the complex band structure emerge away from the real band structure at the extrema of the latter²². Furthermore, the bands emerge with increasing $\text{Re}(\omega_\sigma^2)$ at the maxima of the real band structure and with decreasing $\text{Re}(\omega_\sigma^2)$ at the minima.

We will use this property to construct *vertical bands* that grow monotonously in $\text{Re}(\omega_\sigma^2)$ from zero to infinity. These vertical bands are then used to extract the eigenmodes of each material for a specific frequency in order to match them at an interface plane.

The construction of vertical bands is facilitated by the following: The conditions $\text{Im}(\omega_\sigma^2) > 0$ and $\text{Im}(\omega_\sigma^2) < 0$

divide the complex k_\perp plane into distinct regions. The complex band structure lives on the boundaries of these regions.

D. Algorithm for single sheets

Let us now outline the construction of vertical bands representing the complex band structure for a given k_\parallel . The goal is to obtain sequences of $(\text{Re}(\omega_\sigma^2), \text{Re}(k_\perp), \text{Im}(k_\perp))$, which constitute the ends of the linear line segments of the complex band structure.

We start out evaluating the real band structure, i.e. the eigenvalues of the dynamical matrix with $\text{Im}(k_\perp) = 0$. The eigenvalues provide bands with real-valued, positive ω_σ^2 .

The following steps are performed for each band index σ individually:

1. We start at the first grid point of the real band structure and proceed in one direction along the real k_\perp -axis, accumulating a sequence of k_\perp points and their $\text{Re}(\omega_\sigma^2)$ -values. When an extremum of ω_σ^2 is encountered, we leave the real k_\perp axis and follow the line with $\text{Im}(\omega_\sigma^2)$ into the complex plane. For this purpose, we search the grid points next to the real k_\perp axis for a pair of values with opposite signs of $\text{Im}(\omega_\sigma^2)$. Linear interpolation between this pair yields one end of the line segment which is connected to the extremum of the real band structure on the real axis. This is the first line segment protruding away from the real band structure.
2. From this line segment, the branch is grown to the boundary of the complex k_\perp -grid. This construction is unique: Each line segment of the complex band structure enters a specific triangle. For this triangle, the eigenvalues of ω_σ^2 are known for two corners of the triangle. After diagonalizing the dynamical matrix for the third corner, the linear line segment with $\text{Im}(\omega_\sigma^2) = 0$ within this triangle is calculated analytically from the linearized $\omega_\sigma^2(k)$. If $\text{Im}(\omega_\sigma^2)$ vanishes accidentally at a grid point we change this value $\text{Im}(\omega_\sigma^2)$ artificially to a very small negative value. This modification guarantees that the line segment leads to one of the sides of the triangle and that it does not pass through a grid point. The process of growing the complex band is repeated for the next triangle. The growth process for the complex band ends at the end-points of the grid in the complex k_\perp plane.
3. The complex bands are calculated only for $\text{Im}(k_\perp) \geq 0$. The corresponding branch for $\text{Im}(k_\perp) < 0$ is obtained from the mirror symmetry $\omega_\sigma^2(k_\perp) = (\omega_\sigma^2(k_\perp^*))^*$ of the complex band structure at the plane with $\text{Im}(k_\perp) = 0$. This band, with the points arranged in the opposite order, is the first

section of the next vertical band for this band index σ . It leads back to the real axis, from where we continue to accumulate the k_{\perp} points and $\text{Re}(\omega^2)$ points until we reach the next extremum. From there we again proceed into the complex plane, but now to the same side of the k_{\perp} grid, where this section of the complex band started from.

4. This procedure is repeated until we encounter the end of the real axis. Using periodic boundary conditions, we connect the unfinished band with the first band, which we started from the first grid point on the real k_{\perp} -axis.

Thus we obtain a number of segments of the vertical band structure shown in the bottom of Fig. 7. Each segment starts at the outer boundary of the grid in the complex k_{\perp} plane and proceeds inward to the real k_{\perp} axis. Then it follows from one extremum of the real band structure to the next, from where it turns again back into the complex plane out to the outer boundary. As long as the segments of the vertical band structure stay on one side of the complex plane, their $\text{Re}(\omega^2)$ values either increase or decrease monotonously.

E. Connect different branches

So far, we obtained for each band index σ a number of sections of vertical bands. These sections are now connected between different band indices.

We find that complex bands of two band indices tend to arrive in pairs at the boundary of our k_{\perp} -grid. As in Fig. 6, these two lines first form two halves of a closed line connecting maxima and minima of the real band structure. This circle, however, is not closed but both bands lead nearly straight and parallel away to the outer bounds of our k_{\perp} grid.

We first connect these pairs of lines from different sheets. We make use of the fact that they arrive within the same triangles at the boundary. This leads to vertical bands running over the entire frequency range.

In the following step we remove the loop of spurious bands describing the branch cut, which lead from the circles to the boundary of the complex plane and back. Thus we arrive at a representation of the complex band structure in terms of monotonously increasing vertical bands.

F. Demonstration of the method for a multi-band model

The methodology described above has been applied to the three-band model described in section IV C. The resulting complex band structure is shown in Fig. 7.

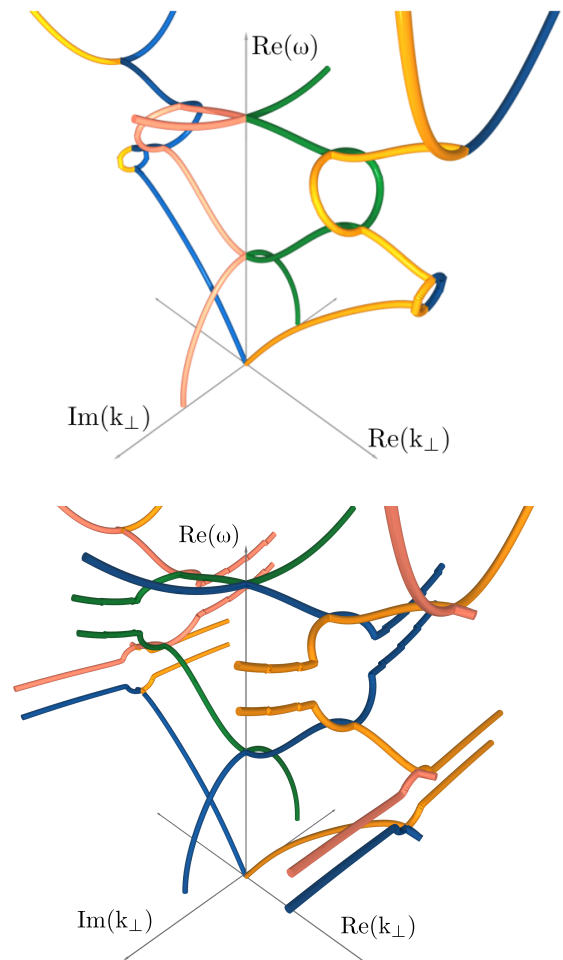


FIG. 7. Top: complex band structure of the three-band model described in section IV C. Different colors indicate different vertical bands of the complex band structure. Bottom: Same as above but before connecting different branches σ . Bands from different branches are shifted vertically away from each other for better visibility. Visible are the spurious bands at the branch cuts.

VI. BEAM MATCHING

Once the complex band structures for the two materials at the interface have been evaluated, the partial solutions from the two materials need to be matched across the interface.

This problem is addressed for a given frequency and \vec{k}_{\parallel} . The vertical bands of the complex band structure provides convenient access to the complex wave vectors $k_{\perp,\alpha}(\omega)$ and the corresponding modes for a given ω . In the following, we will suppress the dependence on ω . We will furthermore use the wave vectors $\vec{k}_{\alpha}(\omega) = \vec{k}_{\parallel} + k_{\perp,\alpha}(\omega)\vec{e}$, where \vec{e} is the interface normal, and where the index α labels the vertical bands in the complex band structure of a given material.

We start with the equations of motion Eq. 14 for the

displacements at the interface, which are Fourier transformed in time.

$$\sum_{j, \vec{t}'} \left(D_{i, \vec{t}, j, \vec{t}'} - \omega^2 \delta_{i, j} \delta_{\vec{t}, \vec{t}'} \right) u_{j, \vec{t}'}(\omega) = 0 \quad (35)$$

For atoms near the interface, the dynamical matrix differs from that in the bulk, because some atoms have changed when forming the interface. Some atoms may be displaced, some have been removed by cutting away one half crystal, and others have been added by attaching the half crystal of the other material.

We insert the ansatz

$$u_{i, \vec{t}}^A = \sum_{\alpha} \frac{1}{\sqrt{m_i}} \bar{U}_{i, \alpha}^A e^{i \vec{k}_{\alpha}^A (\vec{t} - \vec{z}_I)} q_{\alpha}^A \quad (36)$$

$$u_{i, \vec{t}}^B = \sum_{\beta} \frac{1}{\sqrt{m_i}} \bar{U}_{i, \beta}^B e^{i \vec{k}_{\beta}^B (\vec{t} - \vec{z}_I)} q_{\beta}^B \quad (37)$$

for the displacements of the materials A and B into Eq. 35, where \vec{k}_{α}^A is a complex wave vector of material A for the specified frequency ω . The index α identifies the vertical band from which this k -point is obtained. With $\bar{U}_{j, \alpha}^A$ we denote the right-handed eigenvectors of the dynamical matrix $D_{i, j}^A(\vec{k}_{\alpha}^A)$ at the specified frequency ω . The definition for \vec{k}_{β}^B is analogous for material B . The position of the interface plane is z_I .

To simplify the equations of motion Eq. 35 of an atom, we subtract the equation of motion of the respective bulk materials—with the displacements Eq. 36 or Eq. 37 of the respective material. The bulk equation can be subtracted because the ansatz satisfies the bulk equations exactly.

The resulting equations of motion for the displacements $u_{i, \vec{t}}$ of an atom in material A at the interface to material B have the form

$$\sum_{\beta \in B} \left(\sum_{(j, \vec{t}') \in B'} D_{i, \vec{t}, j, \vec{t}'}^{AB} e^{i \vec{k}_{\beta}^B (\vec{t}' - z_I)} \bar{U}_{j, \beta}^B \right) q_{\beta}^B - \sum_{\alpha \in A} \left(\sum_{j, \vec{t}' \in A'} D_{i, \vec{t}, j, \vec{t}'}^A e^{i \vec{k}_{\alpha}^A (\vec{t}' - z_I)} \bar{U}_{j, \alpha}^A \right) q_{\alpha}^A = 0 \quad (38)$$

The sum $(j, \vec{t}') \in B'$ describes the displacements in the material B on the opposite side of the interface. The sum $(j, \vec{t}') \in A'$ runs over all displacements of atoms that have been removed while forming the interface. The sum $\beta \in B$ refers to all vertical bands in the complex band structure of material B , that is all complex k_{\perp} -values at the chosen frequency, and the sum $\alpha \in A$ runs over all vertical bands of material A . Equations analogous to Eq. 38 are set up for atoms in material B at the interface.

These equations are trivially obeyed for displacements $u_{i, \vec{t}}$ for which the matrix elements $D_{i, \vec{t}, j, \vec{t}'}$ of the dynamical matrix are unaffected by the interface.

The equations of motion for the displacements with a changed environment, on the other hand, contribute conditions that link the coefficients q_{α}^A and q_{β}^B of the bulk modes of the two materials.

For the sake of simplicity, we have so far ignored atoms at the interface that can be attributed to none of the two bulk materials. The equation of motion for such an atom contributes three unknowns, the amplitudes u_{γ}^I of the interface atom, and three equations, that link the new coordinates to the coefficients $q_{\alpha}^A, q_{\beta}^B$ of the modes in the bulk materials. The resulting equations are of the same form as Eq. 38, and they are treated analogously.

The resulting set of equations Eq. 38, from the atoms of the atoms of materials A and B at the interface and the interface atoms, has the form of a set of homogeneous linear equations.

$$\sum_j M_{i, j} q_{j, n} = 0 \quad (39)$$

\mathbf{M} is a rectangular, but not square, complex matrix. Its left index runs over all equations of motion that are affected by the interface. The right index of \mathbf{M} runs over all mode amplitudes q_{α}^A and q_{β}^B of both materials and the amplitudes u_{γ}^I of the interface atoms. The index n runs over all independent modes of the interface system.

This problem is equivalent to searching the eigenvectors \vec{q}_n of a matrix \mathbf{M} with vanishing eigenvalue. It is solved with singular-value decomposition, which directly delivers the desired vectors as the null-space of the matrix \mathbf{M} . This null space is spanned by all vectors, that are orthogonal to the rows of the matrix M .

Each vector of the null space provides one set of parameters

$$\vec{q}_j = (\dots, q_{\alpha, j}^A, \dots, u_{\gamma, j}^I, \dots, q_{\beta, j}^B, \dots) \quad (40)$$

where u_{γ}^I are the displacements of those interface atoms that differ from the bulk materials on either side.

A. Transfer matrix

The general solution of Eq. 39 is a superposition $\vec{q} = \sum_j \vec{q}_j c_j$ with arbitrary parameters c_j .

One is often interested in the coefficient transfer matrix $X_{\lambda, \lambda'}$, which provides the coefficients of the modes in one material as linear combination of the mode amplitudes of the other material. The transfer matrix can be obtained from the null vectors Eq. 40 after multiplication with the inverse matrix of null vectors of the incoming channel.

$$X_{\beta, \alpha}^{B \leftarrow A} = \sum_j q_{\beta, j}^B (\mathbf{q}^A)_{j, \alpha}^{-1} \quad (41)$$

The solutions may be of the following types

1. modes that propagate in both materials. They can directly transmit energy through both materials and they contribute to the thermal current.
2. modes that are evanescent in one material but that contain impinging and reflected waves in the other. They do not directly contribute to thermal transport.

3. interface modes, that are evanescent in both directions. These modes exist only near the the interface and they fall off in both directions away from the interface. They describe phonons moving in the interface plane.

These are ideal cases, that are present in their pure form only for simple materials. Usually, the solutions of the interface system combine features of all these special cases.

Modes such as evanescent waves and interface states that do not reach another interface do not contribute to the transmission coefficient. Nevertheless, phonon scattering at impurities or other phonons not considered in the transfer matrix can redistribute their energy into propagating modes, so that they nevertheless contribute indirectly to the thermal current.

B. Beam matching for hanging linear chains

Let us demonstrate the workings of the beam matching for a simple model system of two hanging linear chains with different band widths.

In material A , the parameters for the model are m_A, c_A, b_A , for material B , they are m_B, c_B, b_B . Across the interface connecting the two materials, there is a new spring with force constant c_C . We place the interface such that beads from $j = -\infty$ to $j = 0$ belong to material A , beads from $j = 1$ to $j = +\infty$ belong to material B .

The ansatz for the bulk-like atoms are

$$u_j = \begin{cases} u_j^A & \text{for } j \leq 0 \\ u_j^B & \text{for } j \geq 1 \end{cases} \quad (42)$$

where u_j^A and u_j^B are the displacements of the modes of the bulk materials at the positions ja .

$$\begin{aligned} u_j^A &= \sum_{\alpha=1,2} e^{ik_\alpha^A (aj - z_I)} q_\alpha^A \\ u_j^B &= \sum_{\beta=1,2} e^{ik_\beta^B (aj - z_I)} q_\beta^B \end{aligned} \quad (43)$$

a is the lattice spacing and z_I is the position of the interface. We place the interface in the middle between the two lattice planes, so that its value is $z_I = \frac{1}{2}a$.

There are two equations of motion that are not satisfied by the ansatz for the bulk materials, namely the ones for u_0 and u_1 .

$$\begin{aligned} -m_A \omega^2 u_0 &= -c_A(u_0 - u_{-1}) + c_C(u_1 - u_0) - b_A u_0 \\ -m_B \omega^2 u_1 &= -c_C(u_1 - u_0) + c_B(u_2 - u_1) - b_B u_1 \end{aligned} \quad (44)$$

By subtracting the corresponding bulk equations, we obtain two non-trivial equations

$$\begin{aligned} 0 &= c_C(u_1^B - u_0^A) - c_A(u_1^A - u_0^A) \\ 0 &= -c_C(u_1^B - u_0^A) + c_B(u_1^B - u_0^B) \end{aligned} \quad (45)$$

that correspond to Eq. 38 after inserting the ansatz Eq. 43 for the displacements,.

We arrive at two homogeneous linear equations for four unknowns. The coefficients of these equations form the matrix \mathbf{M} defined in Eq. 39. The two independent solutions spanning the null space of \mathbf{M} provide each a parameter set

$$\vec{q}_j = \left(q_{1,j}^A; q_{2,j}^A; q_{1,j}^B; q_{2,j}^B \right) \quad (46)$$

The superposition of the two vectors gives the general solution for the interface system

$$\begin{pmatrix} q_1^A \\ q_2^A \\ q_1^B \\ q_2^B \end{pmatrix} = \begin{pmatrix} q_{1,1}^A & q_{1,2}^A \\ q_{2,1}^A & q_{2,2}^A \\ q_{1,1}^B & q_{1,2}^B \\ q_{2,1}^B & q_{2,2}^B \end{pmatrix} \begin{pmatrix} q_{1,1}^A & q_{1,2}^A \\ q_{2,1}^A & q_{2,2}^A \end{pmatrix}^{-1} \begin{pmatrix} c_1 \\ c_2 \end{pmatrix} \quad (47)$$

By choosing $c_1 = q_1^A$ and $c_2 = q_2^A$ as initial condition, we can now determine the solution at the interface and in material B .

The transfer matrix \mathbf{X} translates the amplitudes q_α^A in material A into those, q_β^B , of material B via

$$\begin{pmatrix} q_1^B \\ q_2^B \end{pmatrix} = \mathbf{X}^{A \leftarrow B} \begin{pmatrix} q_1^A \\ q_2^A \end{pmatrix} \quad (48)$$

where the transfer matrix is

$$\mathbf{X}^{A \leftarrow B} = \begin{pmatrix} q_{1,1}^B & q_{1,2}^B \\ q_{2,1}^B & q_{2,2}^B \end{pmatrix} \begin{pmatrix} q_{1,1}^A & q_{1,2}^A \\ q_{2,1}^A & q_{2,2}^A \end{pmatrix}^{-1} \quad (49)$$

For the sake of completeness we list the result

$$\mathbf{X}^{A \leftarrow B} = \begin{pmatrix} \frac{M_{4,1}M_{1,2} - M_{1,1}M_{4,2}}{M_{3,1}M_{4,2} - M_{4,1}M_{4,3}} & \frac{M_{2,1}M_{4,2} - M_{4,1}M_{2,2}}{M_{4,1}M_{3,2} - M_{3,1}M_{4,2}} \\ \frac{M_{1,1}M_{3,2} - M_{3,1}M_{1,2}}{M_{3,1}M_{4,2} - M_{4,1}M_{4,3}} & \frac{M_{2,1}M_{4,2} - M_{4,1}M_{2,2}}{M_{4,1}M_{3,2} - M_{3,1}M_{4,2}} \end{pmatrix} \quad (50)$$

with

$$\begin{aligned} M_{1,\alpha} &= -c_A e^{\frac{ik_\alpha^A a}{2}} + (c_A - c_C) e^{-\frac{ik_\alpha^A a}{2}} \\ M_{1,\beta+2} &= c_C e^{\frac{ik_\beta^B a}{2}} \\ M_{2,\alpha} &= c_C e^{-\frac{ik_\alpha^A a}{2}} \\ M_{2,\beta+2} &= -c_B e^{-\frac{ik_\beta^B a}{2}} - (c_B - c_C) e^{\frac{ik_\beta^B a}{2}} \end{aligned} \quad (51)$$

C. Multilayer structures

The transfer matrix of the interface connects the partial solutions on either side of the interface. A second transfer matrix translates the solutions from the left side of a material to the right. Thus, it propagates the solution through the material from one interface to the next.

This matrix is, for material B , given by the complex wave vectors in material B .

$$\mathbf{X}_{\beta,\beta'}^B(d) = \delta_{\beta,\beta'} e^{ik_\beta^B d} \quad (52)$$

where $d := z_{C \leftarrow B} - z_{B \leftarrow A}$ is the distance between the interface planes. Some precaution to prevent over and underflows is required when the wave vectors are complex. A remedy for this problem has been proposed by Ko and Inkson²⁴.

The transfer matrix for the entire multilayer of materials A, B, C, \dots, Z is obtained as the product of the individual transfer matrices as

$$q_{\zeta}^Z = \sum_{\alpha} \left(\mathbf{X}^Z \mathbf{X}^{Z \leftarrow Y} \dots \mathbf{X}^{C \leftarrow B} \mathbf{X}^B \mathbf{X}^{B \leftarrow A} \mathbf{X}^A \right)_{\zeta, \alpha} q_{\alpha}^A \quad (53)$$

The first matrix \mathbf{X}^A propagates the coefficients relative to a given point in contact A to the AB interface, which lies a distance d^A away. Similarly the matrix \mathbf{X}^Z propagates the coefficients from the Y/Z interface to a selected point in contact Z . The other coefficients are all expressed relative to their initial interface. i.e., the A/B interface for the coefficients in material A .

D. Complex band structure of a multilayer structure

One may be interested in a material structure that is in itself repeating, such as a multilayer $\dots ABABA \dots$ of alternating layers of materials A and B . We may consider a repeat unit AB as the unit cell of the composite material and ask for the complex band structure for the composite material. The information about the complex band structure is contained in the transfer matrix of the repeat unit.

Diagonalization of the transfer matrix $X^{ML} := \mathbf{X}^{A \leftarrow B} \mathbf{X}^B \mathbf{X}^{B \leftarrow A} \mathbf{X}^A$ for a given energy and k_{\parallel} yields

$$\left[X_{\lambda', \lambda}^{ML} - e^{ik_{\gamma}^{ML} d_{ML}} \delta_{\lambda', \lambda} \right] q_{\lambda, \gamma}^A(k_{\gamma}^{ML}) = 0 \quad (54)$$

where d_{ML} is the thickness of the repeat unit and k^{ML} is the perpendicular wave vector for the multilayer structure. The eigenvalues $e^{ik_{\gamma}^{ML} d_{ML}}$ provide the complex wave vectors. The real band structure can be constructed selecting modes with real k_{γ} .

The eigenvectors provide the coefficients for the mode in the first material A , and the mode amplitudes of the other materials can be constructed from the corresponding transfer matrices as shown here for material B .

$$q_{\lambda, \gamma}^B(k^{ML}) = \sum_{\lambda' \in A} X_{\lambda, \lambda'}^{B \leftarrow A} q_{\lambda', \gamma}^A(k^{ML}) \quad (55)$$

VII. FROM THE TRANSFER MATRIX TO THE CONDUCTANCE

A. Transmission coefficient

The transfer matrix $X_{\lambda, \lambda'}$ of the complete structure links the amplitudes of the incoming phonon mode λ of

one contact with those of the transmitted phonons in mode λ' .

The mode-resolved transmission coefficient links the outgoing phonon flux in contact B to the incoming phonon fluxes in contact A . The phonon modes λ are labelled as incoming A_i, B_i or outgoing A_o, B_o according to their velocity v_{λ} perpendicular to the interface. If contact B is to the right of contact A , the right-moving phonons in A are incoming and the right-moving contacts in B are outgoing.

$$\begin{pmatrix} \vec{q}^{B_o} \\ \vec{q}^{B_i} \end{pmatrix} = \begin{pmatrix} \mathbf{X}^{B_o \leftarrow A_i} & \mathbf{X}^{B_o \leftarrow A_o} \\ \mathbf{X}^{B_i \leftarrow A_i} & \mathbf{X}^{B_i \leftarrow A_o} \end{pmatrix} \begin{pmatrix} \vec{q}^{A_i} \\ \vec{q}^{A_o} \end{pmatrix} \quad (56)$$

The requirement that there are no incoming currents from contact B , i.e. $\vec{q}^{B_i} = 0$, relates the outgoing phonon currents in B to the incoming currents in contact A .

$$\vec{q}^{B_o} = \mathbf{S}^{B \leftarrow A} \vec{q}^{A_i} \quad (57)$$

The proportionality constant is the corresponding sub-block $\mathbf{S}^{B \leftarrow A}$ of the scattering matrix.

$$\begin{aligned} \mathbf{S}^{B \leftarrow A} &= \mathbf{X}^{B_o \leftarrow A_i} \\ &- \mathbf{X}^{B_o \leftarrow A_o} \left(\mathbf{X}^{B_i \leftarrow A_o} \right)^{-1} \mathbf{X}^{B_i \leftarrow A_i} \end{aligned} \quad (58)$$

The currents are related to the squared amplitudes and the phonon velocities. Thus, the transmission coefficient is

$$\mathcal{T}_{\lambda \in A/in, \lambda' \in B/out} = \frac{1}{n_{\lambda}^0 \vec{e} \vec{v}_{\lambda}} |S_{\lambda, \lambda'}^{B \leftarrow A}|^2 \left(n_{\lambda'}^0 \vec{e} \vec{v}_{\lambda'} \right) \quad (59)$$

Non-propagating modes, those with a finite imaginary part of the wave vector, are excluded from the transmission coefficient, because the net current of all non-propagating modes vanishes.

B. Interface conductance between two cubic spring models

The ballistic interface conductance as defined in Eq. 12 has been analyzed for the interface between two cubic spring models described in section IV B. The two-dimensional band structures of both materials are shown in the bottom of Fig. 8. The parameters have been chosen to visualize the effects of a hard-soft interface.

In order to investigate the conductance, we introduce its density $g(\hbar\omega, \vec{k}_{\parallel})$, which gives the conductance as

$$G = \hbar \int d\omega \int d^2 k_{\parallel} \frac{1}{k_B} C(\hbar\omega, T) g(\hbar\omega, \vec{k}_{\parallel}) \quad (60)$$

where $C(\hbar\omega, T) = \hbar\omega \frac{\partial}{\partial T} \left(e^{\beta\hbar\omega} - 1 \right)^{-1}$ is the contribution of a mode with energy ϵ to the heat capacity and $\beta = 1/(k_B T)$. The function differs only by a constant factor from the one shown in Fig. 1. In the high-temperature

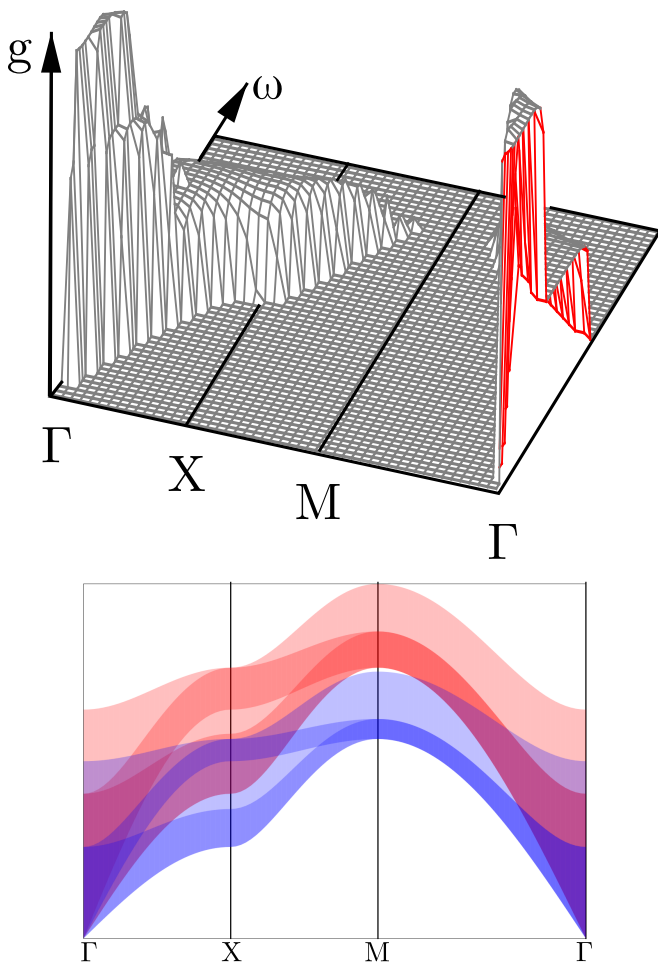


FIG. 8. Top: wave-vector and energy resolved conductance $g(\hbar\omega, \vec{k}_{\parallel})$ of an interface between two cubic spring model systems in the high-temperature limit. At lower temperatures, the contribution of high-energy phonons is suppressed by heat capacity $C_{\lambda}(T)$ shown in Fig. 1. Bottom: two-dimensional band structures $\omega_{\sigma}(\vec{k}_{\parallel})$ for hot material (red) and the cold material B (blue). Darker regions indicate the overlap of several bands with different polarizations.

limit, the contribution of a phonon mode to the heat capacity is a constant.

This density is given by

$$g(\hbar\omega, \vec{k}_{\parallel}) = A_A \sum_{\lambda \in A, \lambda' \in B} k_B n_{\lambda}^0 \cdot (\vec{e}\vec{v}_{\lambda}) \theta(\vec{e}\vec{v}_{\lambda}) \mathcal{T}_{\lambda, \lambda'}^{B \leftarrow A} \times \delta(\hbar\omega - \epsilon_{\lambda}) \delta(\vec{k}_{\parallel} - \vec{k}_{\parallel, \lambda}) \quad (61)$$

Note, that the sum over phonons in contact A translates into a one-dimensional phonon density of states of contact A .

Only the channels $(\omega, \vec{k}_{\parallel})$ in the overlap of the two-dimensional band structures of both materials can transmit heat. This is reflected in the density $g(k_{\parallel}, \omega)$ shown in Fig. 8. It is evident that already this effect cuts off the contribution from the high-frequency part of the spec-

trum. This mechanism, which is temperature independent, supports the notion that the acoustic modes dominate heat transport. The density $g(k_{\parallel}, \omega)$ has a nearly step-like behavior indicating the number of polarizations contributing to the thermal current.

VIII. SUMMARY

We presented a method to calculate the complex band structure of phonons. The strength of this method is its simplicity, because it rests on the diagonalization of the dynamical matrix as the basic element. The method is economical because it explores only those regions in the complex plane, that are visited by the complex band structure. An exception in the current implementation is that branch cuts are still fully explored, a step that can be avoided.

We presented the beam matching of phonon modes at interfaces and multilayers. We demonstrated how it can be used to explore the thermal transport of phonons on the basis of individual phonons, that is, resolved with respect to energy and in-plane wave vectors \vec{k}_{\parallel} .

It has been shown how the three-dimensional real band structure of a multilayer can be constructed from the transfer matrices of the components and their interfaces.

The usual approach for mode-matching⁷⁻⁹ or the calculation of Greens functions²⁻⁵ works selectively at a given frequency at one time. This is very convenient for fermions, for which the transport is restricted to a small energy window at the Fermi level. This advantage is lost in the case of phonons, for which the entire frequency spectrum contributes. Diagonalizing matrices as in the present approach provides the states for the entire spectrum at given wave vector in one step. Instead of scanning over energies for each k_{\parallel} , the present method of calculating the complex band structure scans, for each k_{\parallel} , over lines in the complex k_{\perp} plane.

The present approach differs from slab-based methods²⁻⁹ which divide the material into slabs and then match the slab solutions at each energy. The matrix dimension of the problem is determined by the size of the slab, and the order of the matrix problem is related to the range of the interaction in terms of slabs. The present approach seems to be more economical, because the full translation symmetry of the bulk materials is exploited for the calculation of the bulk complex band structure, while the frequency-dependent matching step is done only once for each interface between different materials.

ACKNOWLEDGMENTS

This work has been supported by the Deutsche Forschungsgemeinschaft through SPP 1386 and project B03 of SFB1073. The authors gratefully acknowledge useful discussions with C. Jooss and C. Volkert

(Göttingen University).

- ¹ P. Kapitza, *J. Phys. USSR* **4**, 181 (1941).
- ² N. Mingo and L. Yang, *Phys. Rev. B* **68**(Dec), 245406 (2003).
- ³ S. Sadasivam, Y. Che, Z. Huang, L. Chen, S. Kumar, and T. S. Fisher, *Ann. Rev. Heat Transfer* **17**, 89 (2014).
- ⁴ J. S. Wang, J. Wang, and J. Lü, *Eur. Phys. J. B* **62**, 381 (2008).
- ⁵ W. Zhang, T. Fisher, and N. Mingo, *Numer. Heat Transfer B* **51**, 333 (2007).
- ⁶ Z. Y. Ong and G. Zhang, *Phys. Rev. B* **91**(May), 174302 (2015).
- ⁷ Y. C. Chang, *Phys. Rev. B* **25**, 605 (1982).
- ⁸ Y. C. Chang and J. N. Schulman, *Phys. Rev. B* **25**, 3975 (1982).
- ⁹ S. k. Yip and Y. C. Chang, *Phys. Rev. B* **30**(Dec), 7037–7059 (1984).
- ¹⁰ R. Peierls, *Ann. Phys.* **3**, 1055 (1929).
- ¹¹ P. Klemens, *Solid State Physics* **7**, 1 (1958).
- ¹² J. E. Turney, E. Landry, A. McGaughey, and C. H. Amon, *Phys. Rev. B* **79**, 64301 (2009).
- ¹³ M. Omini and A. Sparavigna, *Physica B* **212**, 101 (1995).
- ¹⁴ D. Broido, A. Ward, and N. Mingo, *Phys. Rev. B* **72**, 14308 (2005).
- ¹⁵ A. Chernatynskiy and S. Phillpot, *Phys. Rev. B* **82**, 134301 (2010).
- ¹⁶ S. Simons, *Journal of Physics C: Solid State Physics* **7**(22), 4048 (1974).
- ¹⁷ G. Chen, *Phys. Rev. B* **57**(Jun), 14958–14973 (1998).
- ¹⁸ E. S. Landry and A. J. H. McGaughey, *Phys. Rev. B* **80**(Oct), 165304 (2009).
- ¹⁹ S. Merabia and K. Termentzidis, *Phys. Rev. B* **86**(Sep), 094303 (2012).
- ²⁰ I. Tamm, *Phys. Z. Soviet Union* **1**, 733 (1932).
- ²¹ W. Kohn, *Phys. Rev.* **115**, 809 (1959).
- ²² V. Heine, *Proc. Phys. Soc. London* **81**, 300 (1963).
- ²³ E. Blount, *Solid State Phys.* **13**, 305 (1962).
- ²⁴ D. Ko and J. Inkson, *Semicond. Sci. Technol.* **3**, 791 (1988).